PUBLICATIONS OF THE ASTRONOMICAL SOCIETY OF THE PACIFIC, **125**:000–000, 2013 March

A Detailed Model Grid for Solid Planets from 0.1 through 100 Earth Masses

LI ZENG AND DIMITAR SASSELOV
Astronomy Department, Harvard University, Cambridge, MA 02138; lzeng@cfa.harvard.edu, dsasselov@cfa.harvard.edu

Received 2012 July 11; accepted 2013 January 20; published 2013 March 12

ABSTRACT. This article describes a new grid for the mass–radius relation of three-layer exoplanets within the mass range of 0.1–$100\ M_{\oplus}$. The three layers are: Fe (ϵ-phase of iron), $MgSiO_3$ (including both the perovskite phase, post-perovskite phase, and its dissociation at ultrahigh pressures), and H_2O (including Ices Ih, III, V, VI, VII, X, and the superionic phase along the melting curve). We discuss the current state of knowledge about the equations of state (EOS) that influence these calculations and the improvements used in the new grid. For the two-layer model, we demonstrate the utility of contours on the mass–radius diagrams. Given the mass and radius input, these contours can be used to quickly determine the important physical properties of a planet including its $p0$ (central pressure), $p1/p0$ (core–mantle boundary pressure over central pressure), CMF (core mass fraction) or CRF (core radius fraction). For the three-layer model, a curve segment on the ternary diagram represents all possible relative mass proportions of the three layers for a given mass–radius input. These ternary diagrams are tabulated with the intent to make comparison to observations easier. How the presence of Fe in the mantle affects the mass–radius relations is also discussed in a separate section. A dynamic and interactive tool to characterize and illustrate the interior structure of exoplanets built upon models in this article is available online.

Online material: color figures, extended table

1. INTRODUCTION

The transit method of exoplanet discovery has produced a small but well-constrained, sample of exoplanets that are unambiguously solid in terms of interior bulk composition. We call solid planets the ones that possess no H and He envelopes and/or atmospheres, i.e., their bulk radius is determined by elements (and their mineral phases) heavier than H and He. Such solid exoplanets are Kepler-10b (Batalha et al. 2011), CoRoT-7b (Queloz et al. 2009; Hatzes et al. 2011), Kepler-36b (Carter et al. 2012) as well as—most likely—Kepler-20b, e, f; Kepler-18b, and 55 Cnc e, in which the solid material could include high-pressure water ice (see references in § 4.2).

There is an increased interest in comparing observed parameters to current models of interior planetary structure. The models, and their use of approximations and EOS, have evolved since 2005 (Valencia et al. 2006; Fortney et al. 2007; Grasset et al. 2009; Seager et al. 2007; Wagner et al. 2011; Swift et al. 2012), mainly because the more massive solid exoplanets (called super-Earths) have interior pressures that are far in excess of Earth's model, bringing about corresponding gaps in our knowledge of mineral phases and their EOS (see a recent review by Sotin et al. [2010]). Here, we compute a new grid of models in order to aid current comparisons to observed exoplanets on the mass–radius diagram. As in previous such grids, we assume the main constituents inside the planets to be differentiated and model them as layers in one dimension.

The first part of this article aims to solve the two-layer exoplanet model. The two-layer model reveals the underlying physics of planetary interior more intuitively, for which we consider three scenarios: an Fe-$MgSiO_3$, Fe-H_2O, or $MgSiO_3$-H_2O planet.

The current observations generally measure the radius of an exoplanet through transits and the mass through Doppler shift measurement of the host star. For each assumption of core and mantle compositions, given the mass and radius input, the two-layer exoplanet model can be solved uniquely. It is a unique solution of radial dependence of interior pressure and density. As a result, all the characteristic physical quantities, such as the pressure at the center ($p0$), the pressure at core–mantle boundary ($p1$), the core mass fraction (CMF), and the core radius fraction (CRF) naturally fall out from this model. These quantities can be quickly determined by invoking the mass–radius contours.

The next part of this article compares some known exoplanets to the mass–radius curves of six different two-layer exoplanet models: pure Fe, 50% Fe and 50% $MgSiO_3$, pure $MgSiO_3$, 50% $MgSiO_3$ and 50% H_2O, 25% $MgSiO_3$ and 75%H_2O, and pure H_2O. These percentages are in mass fractions. The data of these six curves are available in Table 1.

Up to now, a standard assumption has been that the planet interior is fully differentiated into layers: all the Fe is in the core and all the $MgSiO_3$ is in the mantle. In § 4.3, we will change this assumption and discuss how the presence of Fe in the mantle affects the mass–radius relation.

TABLE 1

DATA FOR THE SIX CHARACTERISTIC MASS—RADIUS CURVES

	Fe		50%Fe-50%$MgSiO_3$				$MgSiO_3\nabla$		50%$MgSiO_3$-50%H_2O				25%$MgSiO_3$-75%H_2O				H_2O	
$\log_{10}(p0)$	Mass[a]	Radius[b]	Mass	Radius	CRF[c]	$p1/p0$[d]	Mass	Radius	Mass	Radius	CRF	$p1/p0$	Mass	Radius	CRF	$p1/p0$	Mass	Radius
09.6	0.001496	0.09947	0.00177	0.121	0.6892	0.2931	0.00623	0.2029	0.008278	0.2963	0.5969	0.2374	0.01217	0.3616	0.4413	0.3782	0.04663	0.58
09.7	0.002096	0.1112	0.002481	0.1354	0.6888	0.2925	0.008748	0.227	0.01156	0.3286	0.6013	0.2398	0.01699	0.4009	0.4444	0.3803	0.06174	0.63
09.8	0.002931	0.1243	0.003472	0.1513	0.6882	0.2918	0.01227	0.254	0.01615	0.3647	0.6051	0.2413	0.02351	0.4432	0.4475	0.385	0.08208	0.6853
09.9	0.00409	0.1387	0.004848	0.169	0.6876	0.2909	0.01717	0.2838	0.02255	0.4049	0.6085	0.242	0.03213	0.4869	0.4513	0.3944	0.1091	0.7455
10.0	0.005694	0.1546	0.006752	0.1885	0.6868	0.2898	0.02399	0.317	0.0313	0.4484	0.6119	0.2446	0.04399	0.535	0.4554	0.4016	0.1445	0.8102
10.1	0.007904	0.1722	0.00938	0.2101	0.6858	0.2886	0.03343	0.3536	0.04314	0.4944	0.6165	0.2495	0.06029	0.588	0.4592	0.4073	0.1904	0.879
10.2	0.01094	0.1915	0.01299	0.2339	0.6847	0.2871	0.04644	0.3939	0.05943	0.5449	0.6209	0.253	0.08255	0.6461	0.4629	0.4119	0.2494	0.9515
10.3	0.01507	0.2126	0.01792	0.26	0.6834	0.2855	0.0643	0.4381	0.0817	0.6003	0.6249	0.2554	0.1127	0.7093	0.4662	0.4159	0.3249	1.028
10.4	0.0207	0.2356	0.02464	0.2886	0.6819	0.2836	0.08866	0.4865	0.112	0.6607	0.6285	0.2571	0.1533	0.7777	0.4693	0.4197	0.4206	1.107
10.5	0.02829	0.2606	0.03372	0.3197	0.6801	0.2815	0.1217	0.5391	0.1528	0.7262	0.6318	0.2585	0.2074	0.8509	0.4721	0.4234	0.5416	1.19
10.6	0.0385	0.2876	0.04595	0.3535	0.6782	0.2792	0.1661	0.596	0.2074	0.7966	0.6347	0.2595	0.2789	0.9289	0.4747	0.427	0.6938	1.276
10.7	0.05212	0.3167	0.06231	0.3901	0.6759	0.2767	0.2255	0.6573	0.2799	0.8718	0.6373	0.2603	0.3726	1.011	0.477	0.4305	0.8866	1.366
10.8	0.07021	0.348	0.08408	0.4296	0.6735	0.274	0.3042	0.7228	0.3754	0.9515	0.6396	0.261	0.4946	1.098	0.4792	0.4339	1.132	1.461
10.9	0.09408	0.3814	0.1129	0.4721	0.6708	0.2711	0.4075	0.7925	0.4998	1.035	0.6416	0.2615	0.6517	1.188	0.4811	0.437	1.444	1.562
11.0	0.1254	0.417	0.1508	0.5177	0.6679	0.2682	0.542	0.8661	0.6607	1.123	0.6434	0.2618	0.8529	1.282	0.4827	0.4397	1.841	1.669
11.1	0.1663	0.4548	0.2003	0.5663	0.6648	0.2651	0.7143	0.9429	0.8653	1.214	0.6448	0.2615	1.107	1.38	0.4839	0.4411	2.346	1.782
11.2	0.2193	0.4949	0.2647	0.618	0.6616	0.2621	0.927	1.02	1.117	1.305	0.6455	0.2598	1.42	1.477	0.4843	0.44	2.985	1.901
11.3	0.2877	0.537	0.348	0.6728	0.6582	0.259	1.2	1.101	1.437	1.4	0.6458	0.2589	1.818	1.58	0.484	0.44	3.77	2.023
11.4	0.3754	0.5814	0.455	0.7307	0.6547	0.2559	1.545	1.186	1.842	1.499	0.6458	0.2582	2.321	1.688	0.4834	0.4403	4.735	2.147
11.5	0.4875	0.6279	0.5919	0.7916	0.6512	0.2529	1.981	1.274	2.351	1.602	0.6453	0.2574	2.957	1.802	0.4828	0.4399	5.909	2.274
11.6	0.6298	0.6765	0.7659	0.8554	0.6476	0.25	2.525	1.365	2.988	1.708	0.6445	0.2565	3.752	1.92	0.4822	0.4391	7.325	2.401
11.7	0.8096	0.727	0.986	0.9221	0.644	0.2473	3.203	1.458	3.78	1.818	0.6435	0.2552	4.732	2.041	0.4813	0.4383	9.038	2.529
11.8	1.036	0.7796	1.261	0.9907	0.6407	0.2451	4.043	1.554	4.763	1.933	0.6423	0.2536	5.936	2.164	0.4803	0.4377	11.11	2.66
11.9	1.319	0.834	1.606	1.062	0.6374	0.2429	5.077	1.653	5.972	2.05	0.641	0.252	7.407	2.289	0.4792	0.4373	13.55	2.789
12.0	1.671	0.8902	2.036	1.136	0.6342	0.2407	6.297	1.749	7.392	2.165	0.6394	0.2488	9.127	2.411	0.4778	0.4341	16.42	2.915
12.1	2.108	0.9481	2.568	1.211	0.631	0.2385	7.714	1.842	9.043	2.275	0.6372	0.2449	11.12	2.529	0.4755	0.4299	19.77	3.039
12.2	2.648	1.007	3.226	1.289	0.6278	0.2363	9.423	1.935	11.03	2.386	0.6345	0.242	13.52	2.647	0.4727	0.4275	23.68	3.16
12.3	3.31	1.068	4.032	1.369	0.6247	0.2342	11.47	2.029	13.4	2.498	0.6317	0.2396	16.37	2.765	0.4695	0.4265	28.21	3.278
12.4	4.119	1.13	5.018	1.451	0.6216	0.2321	13.87	2.121	16.18	2.608	0.6285	0.2371	19.72	2.882	0.467	0.4248	33.49	3.393
12.5	5.103	1.193	6.216	1.534	0.6184	0.23	16.73	2.213	19.48	2.717	0.6252	0.2353	23.68	2.998	0.4646	0.4237	39.62	3.506
12.6	6.293	1.257	7.665	1.618	0.6153	0.228	20.1	2.304	23.36	2.825	0.6219	0.2339	28.31	3.111	0.4623	0.423	46.72	3.616
12.7	7.727	1.321	9.39	1.7	0.6126	0.2267	24.07	2.394	27.94	2.933	0.619	0.2323	33.71	3.222	0.46	0.4225	54.92	3.724
12.8	9.445	1.386	11.45	1.783	0.61	0.2254	28.68	2.483	33.24	3.037	0.6162	0.2306	39.97	3.33	0.4579	0.4214	64.22	3.826
12.9	11.49	1.451	13.91	1.865	0.6074	0.2241	33.99	2.569	39.33	3.138	0.6134	0.2288	47.15	3.434	0.4556	0.4199	74.79	3.924
13.0	13.92	1.515	16.81	1.947	0.6048	0.2227	40.05	2.65	46.26	3.234	0.6105	0.2266	55.31	3.534	0.4531	0.4177	86.85	4.017
13.1	16.78	1.579	20.21	2.027	0.6024	0.2213	46.88	2.728	54.07	3.325	0.6075	0.2238	64.47	3.627	0.4503	0.4148	100.3	4.104
13.2	20.14	1.642	24.2	2.106	0.5999	0.2198	54.49	2.799	62.77	3.409	0.6042	0.2207	74.65	3.713	0.4472	0.4114	115.3	4.183
13.3	24.05	1.704	28.85	2.183	0.5973	0.2182	63.08	2.866	72.58	3.488	0.6006	0.2178	86.14	3.793	0.4438	0.4087	131.9	4.256
13.4	28.6	1.765	34.23	2.258	0.5947	0.2166	72.75	2.928	83.62	3.563	0.5967	0.2152	99.08	3.87	0.4404	0.4064	150.3	4.322
13.5	33.87	1.824	40.45	2.331	0.5921	0.2151	83.59	2.986	95.97	3.631	0.5928	0.2129	113.6	3.94	0.437	0.4043	170.8	4.382
13.6	39.94	1.881	47.59	2.401	0.5895	0.2136	95.68	3.039	109.8	3.695	0.5888	0.2106	129.7	4.006	0.4338	0.4022	193.6	4.435
13.7	46.92	1.937	55.76	2.468	0.5869	0.2123	109.1	3.088	125.1	3.754	0.5847	0.2083	147.6	4.064	0.4306	0.4001	218.7	4.483
13.8	54.93	1.99	65.07	2.531	0.5844	0.2114	124	3.132	142	3.807	0.5807	0.2061	167.2	4.116	0.4274	0.3979	246.6	4.525
13.9	64.08	2.042	75.65	2.59	0.582	0.2106	140.3	3.17	160.6	3.854	0.5768	0.2038	188.8	4.162	0.4242	0.3956	277.3	4.561
14.0	74.51	2.091	87.65	2.645	0.5797	0.21	158.2	3.204	181	3.895	0.5728	0.2015	212.5	4.202	0.4209	0.3932	311.3	4.592
14.1	86.37	2.138	101.2	2.697	0.5775	0.2094	177.8	3.232	203.3	3.93	0.5688	0.1992	238.4	4.236	0.4175	0.3908	348.7	4.618
14.2	99.8	2.183	116.5	2.745	0.5755	0.2089	199.2	3.255	227.7	3.959	0.5648	0.1971	266.8	4.265	0.4142	0.3884	390.1	4.639
14.3	115	2.226	133.8	2.789	0.5735	0.2085	222.5	3.274	254.2	3.983	0.5607	0.1951	297.9	4.288	0.4109	0.3861	435.9	4.656
14.4	132.1	2.266	153.1	2.829	0.5716	0.2082	248.1	3.288	283.3	4.002	0.5567	0.1932	332.1	4.307	0.4076	0.3841	486.4	4.669

[a] Mass in Earth mass ($M_\oplus = 5.9742 \times 10^{24}$ kg).

[b] Radius in Earth radius ($R_\oplus = 6.371 \times 10^6$ m).

[c] CRF stands for core radius fraction, the ratio of the radius of the core over the total radius of the planet, in the two-layer model.

[d] $p1/p0$ stands for core–mantle-boundary pressure fraction, the ratio of the pressure at the core–mantle boundary ($p1$) over the pressure at the center of the planet ($p0$), in the two-layer model.

The final part of this article calculates the three-layer differentiated exoplanet model. Given the mass and radius input, the solution for the three-layer model is non-unique (degenerate), thus a curve on the ternary diagram is needed to represent the set of all solutions. This curve can be obtained by solving differential equations with iterative methods. The ensemble of solutions is tabulated, from which users may interpolate to determine planet composition in three-layer model. A dynamic and interactive tool to characterize and illustrate the interior structure of exoplanets built upon ternary diagrams and other models in this article is available online.[1]

The methods described in this article can be used to rapidly characterize the interior structure of exoplanets.

2. METHOD

Spherical symmetry is assumed in all the models. The interior of a planet is assumed to be fully differentiated into layers in the first part of the paper. The two-layer model consists of a core and a mantle. The three-layer model consists of a core, a mantle, and another layer on top of the mantle. The interior structure is determined by solving the following two differential equations:

$$\frac{dr}{dm} = \frac{1}{4\pi\rho r^2}, \tag{1}$$

$$\frac{dp}{dm} = -\frac{Gm}{4\pi r^4}. \tag{2}$$

The two equations are similar to the ones in Zeng & Seager (2008). However, contrary to the common choice of radius r as the independent variable, the interior mass m is chosen, which is the total mass inside shell radius r, as the independent variable. So the solution is given as $r(m)$ (interior radius r as a dependent function of interior mass m), $p(m)$ (pressure as a dependent function of interior mass m), and $\rho(m)$ (density as a dependent function of interior mass m).

The two differential equations are solved with the EOS of the constituent materials as inputs:

$$\rho = \rho(p, T). \tag{3}$$

The EOS is a material property, which describes the material's density as a function of pressure and temperature. The EOS could be obtained both theoretically and experimentally. Theoretically, the EOS could be calculated by quantum-mechanical molecular dynamics ab initio simulation such as the VASP (Vienna Ab initio Simulation Package) (Kresse & Hafner 1993, 1994; Kresse & Furthmüller 1996; French et al. 2009). Experimentally, the EOS could be determined by high-pressure compression experiment such as the DAC (diamond anvil cell) experiment, or shock wave experiment like the implosion experiment by the Sandia Z-machine (Yu & Jacobsen 2011). The temperature effect on density is secondary compared to the pressure effect (Valencia et al. 2006, 2007b). Therefore, we can safely ignore the temperature dependence of those higher density materials (Fe and $MgSiO_3$) for which the temperature effect is weaker, or we can implicitly include a preassumed pressure-temperature (p-T) relation (for H_2O it is the melting curve) so as to reduce the EOS to a simpler single-variable form:

$$\rho = \rho(p). \tag{4}$$

To solve the set of equations mentioned above, appropriate boundaries conditions are given as:

$p0$: the pressure at the center of the planet

$p1$: the pressure at the first layer interface (the core–mantle boundary)

$p2$: the pressure at the second layer interface (only needed for three-layer model)

p_{surface}: the pressure at the surface of the planet (set to 1 bar [10^5 Pa])

3. EOS OF Fe, $MgSiO_3$ AND H_2O

The three layers that we consider for the planet interior are Fe, $MgSiO_3$, and H_2O. Their detailed EOS are described as follows:

3.1. Fe

We model the core of a solid exoplanet after the Earth's iron core, except that in our model we ignore the presence of all other elements such as nickel (Ni) and light elements such as sulfur (S) and oxygen (O) in the core. As pointed out by Valencia et al. (2010), above 100 GPa, the iron is mostly in the hexagonal closed packed ϵ phase. Therefore, we use the Fe-EOS by Seager et al. (2007). Below $2.09 * 10^4$ GPa, it is a Vinet (Vinet et al. 1987, 1989) formula fit to the experimental data of ϵ-iron at $p \leq 330$ GPa by Anderson et al. (2001). Above $2.09 * 10^4$ GPa, it makes smooth transition to the Thomas–Fermi–Dirac (TFD) EOS (Seager et al. 2007). A smooth transition is assumed because there is no experimental data available in this ultrahigh pressure regime.

The central pressure could reach 250 TPa (terapascals, i.e., 10^{12} Pa) in the most massive planet considered in this article. However, the EOS of Fe above ~1 TPa is beyond the current reach of experiment and thus largely unknown (Swift et al. 2012). Therefore, our best approximation here is to extend the currently available ϵ-iron EOS to higher pressures and connect it to the TFD EOS.

The EOS of Fe is shown in Figure 1 as the upper curve.

---

[1] See http://www.cfa.harvard.edu/~lzeng/.

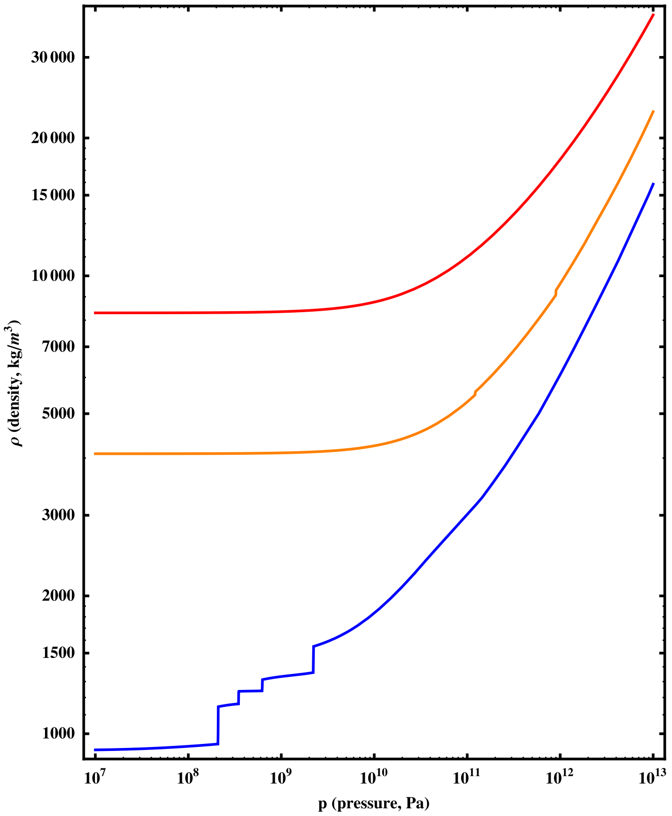

FIG. 1.—$p - \rho$ EOS of Fe (ϵ-phase of iron, *red curve*), $MgSiO_3$ (perovskite phase, post-perovskite phase and its high-pressure derivatives, *orange curve*), and H_2O (Ice Ih, Ice III, Ice V, Ice VI, Ice VII, Ice X, and superionic phase along its melting curve, i.e., solid–liquid phase boundary) See the online edition of the *PASP* for a color version of this figure.

3.2. $MgSiO_3$

We model the silicate layer of a solid exoplanet using the Earth's mantle as a proxy. The FeO-free Earth's mantle with $Mg/Si = 1.07$ would consist of mainly enstatite ($MgSiO_3$) or its high-pressure polymorphs and, depending upon pressure, small amounts of either forsterite and its high-pressure polymorphs (Mg_2SiO_4) or periclase (MgO) (e.g., Bina 2003).

The olivine polymorphs, as well as lower-pressure enstatite and majorite ($MgSiO_3$ with garnet structure), are not stable above 27 GPa. At higher pressures, the system would consist of $MgSiO_3$-perovskite (pv) and periclase or their higher-pressure polymorphs (Stixrude & Lithgow-Bertelloni 2011; Bina 2003). Given the high pressures at the H_2O-silicate boundary usually exceeding 27 GPa, we can safely ignore olivine and lower-pressure pyroxene polymorphs. For the sake of simplicity, we also ignore periclase, which would contribute only 7 at.% to the silicate mantle mineralogical composition (Bina 2003). There are also small amounts of other elements such as aluminum (Al), calcium (Ca), and sodium (Na) present in Earth's mantle (Sotin et al. 2007). For simplicity, we neglect them and thus the phases containing them are not included in our model. We also do not consider SiC because carbon-rich planets might form under very rare circumstances, and are probably not common.

Some fraction of Fe can be incorporated into the minerals of the silicate mantle, which could then have the general formula as $(Mg, Fe)SiO_3$. For now, we simply assume all the Fe is in the core and all the Mg is in the mantle in the form of $MgSiO_3$-perovskite and/or its high-pressure polymorphs; thus the planet is fully differentiated. In a later section, we will discuss how the addition of Fe to the mantle can affect mass–radius relation and compare the differences between differentiated and undifferentiated as well as reduced and oxidized planets in § 4.3.

We first consider the perovskite (pv) and post-perovskite (ppv) phases of pure $MgSiO_3$. $MgSiO_3$ perovskite (pv) is believed to be the major constituent of the Earth mantle. It makes transition into the post-perovskite (ppv) phase at roughly 120 GPa and 2500 K (corresponding to a depth of 2600 km in Earth) (Hirose 2010). The ppv phase was discovered experimentally in 2004 (Murakami et al. 2004) and was also theoretically predicted in the same year (Oganov & Ono 2004). The ppv is about 1.5% denser than the pv phase (Caracas & Cohen 2008; Hirose 2010). This 1.5% density jump resulting from the pv-to-ppv phase transition can be clearly seen as the first density jump of the $MgSiO_3$ EOS curve shown in Figure 1. Both the $MgSiO_3$ pv EOS and $MgSiO_3$ ppv EOS are taken from Caracas & Cohen (2008). The transition pressure is determined to be 122 GPa for pure $MgSiO_3$ according to Spera et al. (2006).

Beyond 0.90 TPa, $MgSiO_3$ ppv undergoes a two-stage dissociation process predicted from the first-principle calculations by Umemoto & Wentzcovitch (2011). $MgSiO_3$ ppv first dissociates into CsCl-type MgO and $P2_1$c-type $MgSi_2O_5$ at the pressure of 0.90 TPa, and later into CsCl-type MgO and Fe_2 P-type SiO_2 at pressures higher than 2.10 TPa. The EOS of CsCl-type MgO, $P2_1$c-type $MgSi_2O_5$, and Fe_2P-type SiO_2 are adopted from Umemoto & Wentzcovitch (2011) and Wu et al. (2011). Therefore, there are two density jumps at the dissociation pressures of 0.90 and 2.10 TPa. The first one can be seen clearly in Figure 1. The second one cannot be seen in Figure 1 since it is too small, but it surely exists.

Since Umemoto & Wentzcovitch's (2011) EOS calculation applies only up to 4.90 TPa, beyond 4.90 TPa, a modified version of the EOS by Seager et al. (2007) is used to smoothly connect to the TFD EOS. TFD EOS assumes electrons in a slowly varying potential with a density-dependent correlation energy term that describes the interactions among electrons. It is therefore insensitive to any crystal structure or arrangements of atoms and it becomes asymptotically more accurate at higher pressure. Thus, the TFD EOS of $MgSiO_3$ would be no different from the TFD EOS of MgO plus SiO_2 as long as the types and numbers of atoms in the calculation are the same. So it is safe to use the TFD EOS of $MgSiO_3$ as an approximation of the EOS of MgO and SiO_2 mixture beyond 4.90 TPa here.

Seager et al.'s (2007) EOS is calculated from the method of Salpeter & Zapolsky (1967) above $1.35 * 10^4$ GPa. Below $1.35 * 10^4$ GPa, it is a smooth connection to TFD EOS from the fourth-order Birch-Murbaghan Equation of State (BME) (see Birch 1947; Poirier 2000) fit to the parameters of $MgSiO_3$ pv obtained by ab initio lattice dynamics simulation of Karki et al. (2000).

Seager et al.'s EOS is slightly modified to avoid any artificial density jump when connected with Umemoto & Wentzcovitch's EOS at 4.90 TPa. At 4.90 TPa, the ratio of the density ρ between Umemoto & Wentzcovitch's EOS and Seager et al.'s EOS is 1.04437. This ratio is multiplied to the original Seager et al.'s EOS density ρ to produce the actual EOS used in our calculation for $p > 4.90$ TPa. A smooth transition is assumed because no experimental data is available in this ultrahigh-pressure regime. This assumption does not affect our low or medium mass planet models, since only the most massive planets in our model could reach this ultrahigh pressure in their $MgSiO_3$ part.

The EOS of $MgSiO_3$ is shown in Figure 1 as the middle curve.

3.3. H_2O

The top layer of a planet could consist of various phases of H_2O. Since H_2O has a complex phase diagram, and it also has a stronger temperature dependence, the temperature effect cannot be ignored. Instead, we follow the solid phases along the melting curve (solid–liquid phase boundary on the p-T plot by Chaplin [2012]). Along the melting curve, the H_2O undergoes several phase transitions. Initially, it is Ice Ih at low pressure, then subsequently transforms into Ice III, Ice V, Ice VI, Ice VII, Ice X, and superionic phase (Chaplin 2012; Choukroun & Grasset 2007; Dunaeva et al. 2010; French et al. 2009).

3.3.1. Chaplin's EOS

The solid form of water has very complex phases in the low-pressure and low-temperature regime. These phases are well determined by experiments. Here we adopt the Chaplin's EOS for Ice Ih, Ice III, Ice V, and Ice VI below 2.216 GPa (see Chaplin 2012; Choukroun & Grasset 2007; Dunaeva et al. 2010). Along the melting curve (the solid–liquid boundary on the p-T diagram), the solid form of water first exists as Ice Ih (hexagonal ice) from ambient pressure up to 209.5 MPa (Choukroun & Grasset 2007). At the triple point of 209.5 MPa and 251.15 K (Choukroun & Grasset 2007; Robinson et al. 1996), it transforms into Ice III (Ice-three), whose unit cell forms tetragonal crystals. Ice III exists up to 355.0 MPa and transforms into a higher-pressure form Ice V (Ice-five) at the triple point of 355.0 MPa and 256.43 K (Choukroun & Grasset 2007). Ice V's unit cell forms monoclinic crystals. At the triple point of 618.4 MPa and 272.73 K (Choukroun & Grasset 2007), Ice V transforms into yet another higher-pressure form Ice VI (Ice-six). Ice VI's unit cell forms tetragonal crystals. A single molecule in Ice VI crystal is bonded to four other water molecules. Then at the triple point of 2.216 GPa and 355 K (Daucik & Dooley 2011), Ice VI transforms into Ice VII (Ice-seven). Ice VII has a cubic crystal structure. Ice VII eventually transforms into Ice X (Ice-ten) at the triple point of 47 GPa and 1000 K (Goncharov et al. 2005). In Ice X, the protons are equally spaced and bonded between the oxygen atoms, where the oxygen atoms are in a body-centered cubic lattice (Hirsch & Holzapfel 1984). The EOS of Ice X and Ice VII are very similar. For Ice VII (above 2.216 GPa), we switch to Frank, Fei, & Hu's EOS (Frank et al. [2004], hereafter FFH2004).

3.3.2. FFH2004's EOS

We adopt FFH2004's EOS of Ice VII for 2.216 GPa $\leq p \leq 37.4$ GPa. This EOS is obtained using the Mao-Bell type diamond anvil cell with an external Mo-wire resistance heater. Gold and water are put into the sample chamber and compressed. The diffraction pattern of both H_2O and gold are measured by the energy-dispersive X-ray diffraction (EDXD) technique at the Brookhaven National Synchrotron Light Source. The gold here is used as an internal pressure calibrant. The disappearance of the diffraction pattern of the crystal Ice VII is used as the indicator for the solid–liquid boundary (melting curve). The melting curve for Ice VII is determined accurately from 3 to 60 GPa and fit to a Simon equation. The molar density (ρ in mol cm^{-3}) of Ice VII as a function of pressure (p in GPa) is given by the following formula in FFH2004:

$$\rho\,(\mathrm{mol\ cm}^{-3}) = 0.0805 + 0.0229 * (1 - \exp^{-0.0743*p}) + 0.1573 * (1 - \exp^{-0.0061*p}). \tag{5}$$

We use equation (5) to calculate ρ from 2.216 GPa up to 37.4 GPa. The upper limit 37.4 GPa is determined by the intersection between FFH2004's EOS and French et al.'s EOS (French et al. [2009], hereafter FMNR2009).

3.3.3. FMNR2009's EOS

FMNR2009's EOS is used for Ice VII, Ice X, and superionic phase of H_2O for 37.4 GPa $\leq p \leq 8.893$ TPa. This EOS is determined by quantum-molecular dynamics simulations using the Vienna Ab Initio Simulation Package (VASP). The simulation is based on finite temperature density-functional theory (DFT) for the electronic structure and treating the ions as classical particles. Most of French et al.'s simulations consider 54 H_2O molecules in a canonical ensemble, with the standard VASP PAW potentials, the 900 eV plane-wave cutoff, and the evaluation of the electronic states at the Γ point considered, for the three independent variables: temperature (T), volume (V), and particle number (N). The simulation results are the thermal EOS $p(T, V, N)$, and the caloric EOS $U(T, V, N)$. The data are tabulated in FMNR2009.

In order to approximate density ρ along the melting curve, from Table V in FMNR2009, we take one data point from Ice VII phase at 1000 K and $2.5\ \mathrm{g\,cm^{-3}}$, four data points from Ice X phase at 2000 K and $3.25\ \mathrm{g\,cm^{-3}}$ to $4.00\ \mathrm{g\,cm^{-3}}$, and the rest of the data points from the superionic phase at 4000 K and $5.00\ \mathrm{g\,cm^{-3}}$ up to $15\ \mathrm{g\,cm^{-3}}$. Since the temperature effect on density becomes smaller towards higher pressure, all the isothermal pressure–density curves converge on the isentropic pressure–density curves as well as the pressure–density curve along the melting curve.

The FMNR2009's EOS has been confirmed experimentally by Thomas Mattson et al. at the Sandia National Laboratories. At 8.893 TPa, FMNR2009's EOS is switched to the TFD EOS in Seager et al. (2007) (hereafter SKHMM2007).

3.3.4. SKHMM2007's EOS

At ultrahigh pressure, the effect of electron–electron interaction can be safely ignored and electrons can be treated as a gas of noninteracting particles that obey the Pauli exclusion principle subject to the Coulomb field of the nuclei. Assuming the Coulomb potential is spatially slowly varying throughout the electron gas that the electronic wave functions can be approximated locally as plane waves, the so-called TFD solution could be derived so that the Pauli exclusion pressure balances out the Coulomb forces (Eliezer et al. 2002; Macfarlane 1984).

In SKHMM2007, a modified TFD by Salpeter & Zapolsky (1967) is used. It is modified in the sense that we have added in a density-dependent correlation energy term which characterizes electron interaction effects.

Here, Seager et al.'s EOS is slightly modified to connect to the FMNR2009's EOS. At 8.893 TPa, the ratio of the density ρ between the FMNR2009's EOS and Seager et al.'s EOS is 1.04464. This ratio is multiplied to the original Seager et al.'s EOS density ρ to produce the actual EOS used in our calculation for $p > 8.893$ TPa. Only the most massive planets in our model could reach this pressure in the H_2O layer, so this choice of EOS for $p > 8.893$ TPa has small effect on the overall mass–radius relation to be discussed in the next section.

The EOS of H_2O is shown in Figure 1 as the lower curve.

4. RESULTS

4.1. Mass–Radius Contours

Given mass and radius input, various sets of mass–radius contours can be used to quickly determine the characteristic interior structure quantities of a two-layer planet including its $p0$ (central pressure), $p1/p0$ (ratio of core–mantle boundary pressure over central pressure), CMF (core mass fraction), and CRF (core radius fraction).

The two-layer model is uniquely solved and represented as a point on the mass–radius diagram given any pair of two parameters from the following list: M (mass), R (radius), $p0$, $p1/p0$, CMF, CRF, etc. The contours of constant M or R are trivial on the mass–radius diagram, which are simply vertical or horizontal lines. The contours of constant $p0$, $p1/p0$, CMF, or CRF are more useful.

Within a pair of parameters, fixing one and continuously varying the other, the point on the mass–radius diagram moves to form a curve. Multiple values of the fixed parameter give multiple parallel curves forming a set of contours. The other set of contours can be obtained by exchanging the fixed parameter for the varying parameter. The two sets of contours crisscross each other to form a mesh, which is a natural coordinate system (see Fig. 2) of this pair of parameters, superimposed onto the existing Cartesian (M, R) coordinates of the mass–radius diagram. This mesh can be used to determine the two parameters given the mass and radius input or vice versa.

4.1.1. Fe-$MgSiO_3$ *Planet*

As an example, the mesh of $p0$ with $p1/p0$ for an Fe-core $MgSiO_3$-mantle planet is illustrated in the first subplot (*upper left*) of Figure 2. The mesh is formed by $p0$-contours and $p1/p0$-contours crisscrossing each other. The more vertical set of curves represents the $p0$-contours. The ratio of adjacent $p0$-contours is $10^{0.1}$ (see Table 1). The more horizontal set of curves represents the $p1/p0$-contours. From bottom up, the $p1/p0$ values vary from 0 to 1 with step size 0.1.

Given a pair of $p0$ and $p1$ input, users may interpolate from the mesh to find the mass and radius. On the other hand, given the mass and radius of a planet, users may also interpolate from the mesh to find the corresponding $p0$ and $p1$ of a two-layer, Fe-core $MgSiO_3$-mantle planet.

Similarly, the contour mesh of $p0$ with CMF for the Fe-$MgSiO_3$ planet is shown as the middle panel in the top row of Figure 2. As a reference point, for a pure-Fe planet with $p0 = 10^{11}$ Pa, $M = 0.1254\ M_\oplus$, $R = 0.417\ R_\oplus$.

The contour mesh of $p0$ with CRF for the Fe-$MgSiO_3$ planet is shown as the right panel of the top row of Figure 2.

4.1.2. $MgSiO_3$-H_2O *Planet*

For two-layer $MgSiO_3$-H_2O planet, the three diagrams ($p0$ contours pair with $p1/p0$ contours, CMF contours, or CRF contours) are the subplots of the middle row of Figure 2.

As a reference point, for a pure-$MgSiO_3$ planet with $p0 = 10^{10.5}$ Pa, $M = 0.122\ M_\oplus$, $R = 0.5396\ R_\oplus$.

4.1.3. Fe-H_2O *Planet*

For two-layer Fe-H_2O planet, the three diagrams ($p0$ contours pair with $p1/p0$ contours, CMF contours, or CRF contours) are the subplots of the bottom row of Figure 2.

As a reference point, for a pure-Fe planet with $p0 = 10^{11}$ Pa, $M = 0.1254\ M_\oplus$, $R = 0.417\ R_\oplus$.

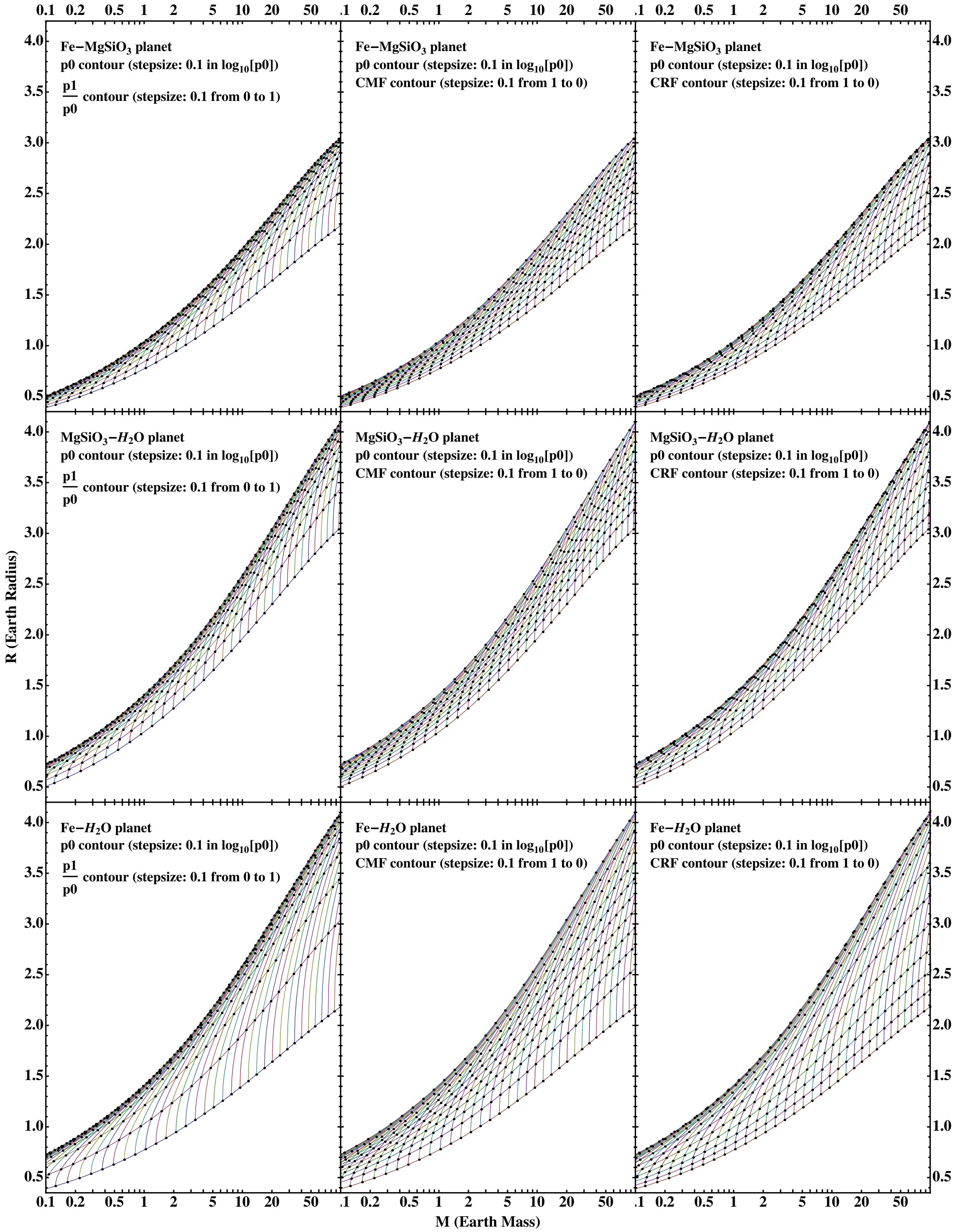

FIG. 2.—Mass–radius contours of two-layer planet. *Top*: Fe-MgSiO$_3$ planet. *Middle row*: MgSiO$_3$-H$_2$O planet. *Bottom*: Fe-H$_2$O planet. *Left*: contour mesh of $p1/p0$ with $p0$. *Middle column*: contour mesh of CMF with $p0$. *Right*: contour mesh of CRF with $p0$. To find out what $p0$ value each $p0$-contour corresponds to, please refer to Table 1. See the online edition of the *PASP* for a color version of this figure.

4.2. Mass–Radius Curves

For observers' interest, six characteristic mass–radius curves are plotted (Fig. 3) and tabulated (Table 1), representing the pure-Fe planet, half-Fe half-$MgSiO_3$ planet, pure $MgSiO_3$ planet, half-$MgSiO_3$ half-H_2O planet, $75\%H_2O$-$25\%MgSiO_3$ planet, and pure H_2O planet. These fractions are mass fractions. Figure 3 also shows some recently discovered exoplanets within the relevant mass–radius regime for comparison. These planets include Kepler-10b (Batalha et al. 2011), Kepler-11b (Lissauer et al. 2011), Kepler-11f (Lissauer et al. 2011), Kepler-18b (Cochran et al. 2011), Kepler-36b (Carter et al. 2012), and Kepler-20b, c, d (Gautier et al. 2012). They also include Kepler-20e ($R = 0.868^{+0.074}_{-0.096}\ R_{\oplus}$ [Fressin et al. 2012], the mass range is determined by pure-silicate mass–radius curve and the maximum collisional stripping curve [Marcus et al. 2010]), Kepler-20f ($R = 1.034^{+0.100}_{-0.127}\ R_{\oplus}$ [Fressin et al. 2012], the mass range is determined by 75% water-ice and 25% silicate mass–radius curves and the maximum collisional stripping curve [Marcus et al. 2010]), Kepler-21b ($R = 1.64 \pm 0.04\ R_{\oplus}$ [Howell et al. 2012]; the upper limit for mass is $10.4\ M_{\oplus}$: the 2- σ upper limit preferred in the paper; the lower limit is $4\ M_{\oplus}$, which is in between the "Earth" and "$50\%H_2O$-$50\%MgSiO_3$" model curves—the planet is very hot and is unlikely to have much water content, if any at all.), Kepler-22b ($R = 2.38 \pm 0.13\ R_{\oplus}$ [Borucki et al. 2012]; the 1- σ upper limit for mass is $36\ M_{\oplus}$ for an eccentric orbit, or $27\ M_{\oplus}$, for circular orbit), CoRoT-7b ($M = 7.42 \pm 1.21\ M_{\oplus}$, $R = 1.58 \pm 0.1\ R_{\oplus}$ [Hatzes et al. 2011; Leger et al. 2009; Queloz et al. 2009]), 55 Cancri e ($M = 8.63 \pm 0.35\ M_{\oplus}$, $R = 2.00 \pm 0.14\ R_{\oplus}$ [Winn et al. 2011]), and GJ 1214b (Charbonneau et al. 2009).

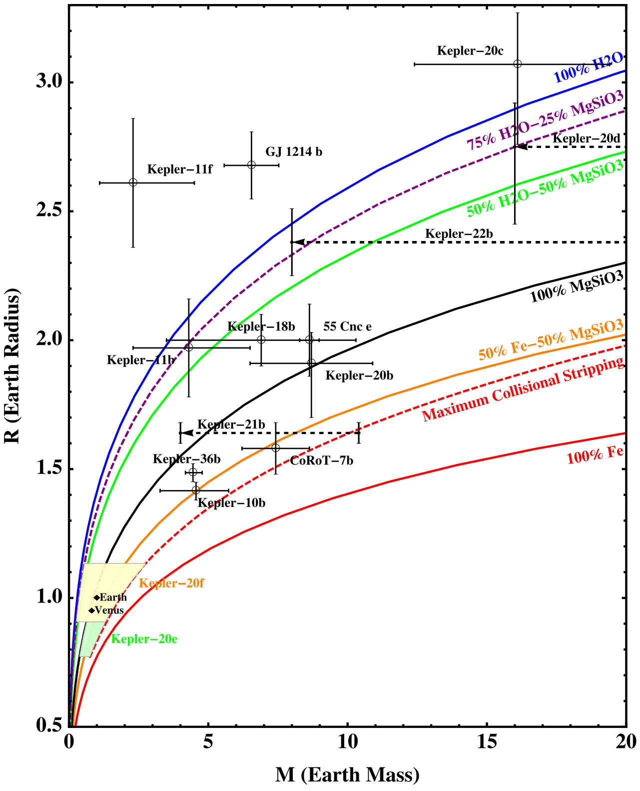

FIG. 3.—Currently known transiting exoplanets are shown with their measured mass and radius with observation uncertainties. Earth and Venus are shown for comparison. The curves are calculated for planets composed of pure Fe, 50% Fe-50% $MgSiO_3$, pure $MgSiO_3$, 50% H_2O-50% $MgSiO_3$, 75% H_2O-25% $MgSiO_3$, and pure H_2O. The *red dashed curve* is the maximum collisional stripping curve calculated by Marcus et al. (2010). See the online edition of the *PASP* for a color version of this figure.

4.3. Levels of Planet Differentiation: The Effect of Fe Partitioning Between Mantle and Core

All models of planets discussed so far assume that all Fe is in the core, while all Mg, Si and O are in the mantle, i.e., that a planet is fully differentiated. However, we know that in terrestrial planets some Fe is incorporated into the mantle. There are two separate processes which affect the Fe content of the mantle: (1) mechanical segregation of Fe-rich metal from the mantle to the core, and (2) different redox conditions resulting in a different Fe/Mg ratio within the mantle, which in turn affects the relative size of the core and mantle. In this section we show the effects of (1) undifferentiated versus fully-differentiated, and (2) versus oxidized planetary structure on the mass–radius relation for a planet with the same Fe/Si and Mg/Si ratios.

For simplicity, here we ignore the H_2O and gaseous content of the planet and only consider the planet as made of Fe, Mg, Si, O. To facilitate comparison between different cases, we fix the global atomic ratios of $Fe/Mg = 1$ and $Mg/Si = 1$; these fit well within the range of local stellar abundances (Grasset et al. 2009).

In particular, we consider a double-layer planet with a core and a mantle in two scenarios. One follows the incomplete mechanical separation of the Fe-rich metal during planet formation, and results in addition of Fe to the mantle as metal particles. It does not change EOS of the silicate components, but requires adding an Fe-EOS to the mantle mixture. Thus, the planet generally consists of a Fe metal core and a partially differentiated mantle consisting of the mixture of metallic Fe and $MgSiO_3$ silicates. While the distribution of metallic Fe may have a radial gradient, for simplicity we assume that it is uniformly distributed in the silicate mantle. Within scenario 1, we calculate three cases to represent different levels of differentiation:

Case 1: complete differentiation—Metallic Fe core and $MgSiO_3$ silicate mantle. For $Fe/Mg = 1$, $CMF = 0.3574$.

Case 2: partial differentiation—Half the Fe forms a smaller metallic Fe core, with the other half of metal being mixed with $MgSiO_3$ silicates in the mantle. $CMF = 0.1787$.

Case 3: no differentiation—All the metallic Fe is mixed with $MgSiO_3$ in the mantle. $CMF = 0$ (no core).

The other scenario assumes different redox conditions, resulting in different Fe/Mg ratios in mantle minerals, and therefore requiring different EOS for the Fe^{2+}-bearing silicates and oxides. More oxidized mantle means adding more Fe in the form of FeO to the $MgSiO_3$ silicates to form $(Mg, Fe)SiO_3$ silicates and (Mg,Fe)O magnesiowüstite (mv), thus reducing the amount of Fe in the core. The exact amounts of $(Mg, Fe)SiO_3$ and (Mg,Fe)O in the mantle are determined by the following mass balance equation:

$$x\mathrm{FeO} + \mathrm{MgSiO_3} \rightarrow (\mathrm{Mg}_{\frac{1}{1+x}}, \mathrm{Fe}_{\frac{x}{1+x}})\mathrm{SiO_3} + x(\mathrm{Mg}_{\frac{1}{1+x}}, \mathrm{Fe}_{\frac{1}{1+x}})\mathrm{O}, \tag{6}$$

where$x$ denotes the relative amount of FeO added to the silicate mantle, $x = 0$ being the most reduced state with no Fe in the mantle, and $x = 1$ being the most oxidized state with all Fe existing as oxides in the mantle. This oxidization process conserves the global Fe/Mg and Mg/Si ratios, but increases O content and thus the O/Si ratio of the planet since Fe is added to the mantle in the form of FeO. Because in stellar environments O is excessively abundant relative to Mg, Si, and Fe (e.g., the solar elemental abundances [Asplund et al. 2009]), it is not a limiting factor in our models of oxidized planets. We calculate the following three cases to represent the full range of redox conditions:

Case 4: no oxidization of Fe—$x = 0$. Metal Fe core and $MgSiO_3$ silicate mantle. For $\mathrm{Fe/Mg} = 1$, $\mathrm{O/Si} = 3$, $\mathrm{CMF} = 0.3574$.

Case 5: partial oxidization of Fe—$x = 0.5$. Half the Fe forms smaller metal core, the other half is added as FeO to the mantle. $\mathrm{O/Si} = 3.5$, $\mathrm{CMF} = 0.1700$.

Case 6: complete oxidization of Fe—$x = 1$. All Fe is added as FeO to the mantle, resulting in no metal core at all. $\mathrm{O/Si} = 4$, $\mathrm{CMF} = 0$.

Notice that Case 4 looks identical to Case 1. However, the silicate EOS used to calculate Case 4 is different from Case 1 at ultrahigh pressures (beyond 0.90 TPa). For Cases 4, 5, and 6, the $(Mg, Fe)SiO_3$ EOS is adopted from Caracas & Cohen (2008) and Spera et al. (2006) which only consider perovskite (pv) and post-perovskite (ppv) phases without including further dissociation beyond 0.90 TPa, since the Fe^{2+}-bearing silicate EOS at ultrahigh pressures is hardly available. On the other hand, comparison between Case 1 and Case 4 also shows the uncertainty on mass–radius relation resulting from the different choice of EOS (see Table 2). Fe^{2+}-bearing pv and ppv have the general formula: $(Mg_y, Fe_{1-y})SiO_3$, where y denotes the relative atomic number fraction of Mg and Fe in the silicate mineral. The $(Mg_y, Fe_{1-y})SiO_3$ silicate is therefore a binary component equilibrium solid solution. It could either be pv or ppv or both depending on the pressure (Spera et al. 2006). We can safely approximate the narrow pressure region where pv and ppv co-exist as a single transition pressure from pv to ppv. This pressure is calculated as the arithmetic mean of the initial transition pressure of pv → pv + ppv mixture and the final transition pressure of pv + ppv mixture → ppv (Spera et al. 2006). The pv EOS and ppv EOS are connected at this transition pressure to form a consistent EOS for all pressures.

Addition of FeO to $MgSiO_3$ results in the appearance of a second phase, magnesiowüstite, in the mantle according to equation 6. The (Mg,Fe)O EOS for Cases 4, 5, and 6 is adopted from Fei et al. (2007), which includes the electronic spin transition of high-spin to low-spin in Fe^{2+}. For simplicity, we assume that pv/ppv and mw have the same Mg/Fe ratio.

Figure 4 shows fractional differences (η) in radius of Cases 2 and 3 compared to Case 1 as well as Cases 5 and 6 compared to Case 4 (r_0 is radius of the reference case, which is that of Case 1 for Cases 2 and 3 and is that of Case 4 for Cases 5 and 6):

$$\eta = \frac{r - r_0}{r_0}. \tag{7}$$

Oxidization of Fe (partitioning Fe as Fe-oxides from the core into the mantle) makes the planet appear larger. The complete oxidization of Fe makes the radius 3% larger for small planets around 1 $M_\oplus$, then the difference decreases with increasing mass within the mass range of 1 to 20 $M_\oplus$. Undifferentiated planets (partitioning of metallic Fe from the core into the mantle) appear smaller than fully differentiated planets. The completely undifferentiated planet is practically indistinguishable in radius for small planets around 1 $M_\oplus$, then the difference increases to 1%-level around 20 $M_\oplus$. The mass, radius, CRF and $p1/p0$ data of Cases 1 through 6 are listed in Table 2.

4.4. Tabulating the Ternary Diagram

For the three-layer model of solid exoplanet, points of a curve segment on the ternary diagram represent all the solutions for a given mass–radius input. These ternary diagrams are tabulated (Table 3) with the intent to make comparison to observations easier.

Usually, there are infinite combinations (solutions) of Fe, $MgSiO_3$, and H_2O mass fractions which can give the same mass–radius pair. All the combinations together form a curve segment on the ternary diagram of Fe, $MgSiO_3$, and H_2O mass fractions (Zeng & Seager 2008; Valencia et al. 2007a). This curve segment can be approximated by three points on it: two endpoints where one or more out of the three layers are absent and one point in between where all three layers are present to give the same mass and radius. The two endpoints correspond to the minimum central pressure ($p0_{\mathrm{min}}$) and maximum central pressure ($p0_{\mathrm{max}}$) allowed for the given mass–radius pair. The middle point is chosen to have the central pressure $p0_{\mathrm{mid}} = \sqrt{p0_{\mathrm{max}} * p0_{\mathrm{min}}}$.

Table 3 contains eight columns:

1. *Mass*. The masses range from 0.1 to 100 $M_\oplus$ with 41 points in total. The range between 0.1 and 1 $M_\oplus$ is equally divided into 10 sections in logarithmic scale. The range between 1 and 10 $M_\oplus$ is equally divided into 20 sections in logarithmic

TABLE 2

DATA OF CASES 1–6

	Case 1 (CMF = 0.3574)				Case 2 (CMF = 0.1787)				Case 3		Case 4 (CMF = 0.3574)				Case 5 (CMF = 0.1700)				Case 6	
$\log_{10}(p0)$	Mass[a]	Radius[b]	CRF[c]	$p1/p0$[d]	Mass	Radius	CRF	$p1/p0$	Mass	Radius	Mass	Radius	CRF	$p1/p0$	Mass	Radius	CRF	$p1/p0$	Mass	Radius
9.6 ……	0.002009	0.1302	0.5972	0.3847	0.002395	0.1381	0.4736	0.5634	0.004165	0.1659	0.002009	0.1302	0.5972	0.3847	0.002526	0.1428	0.4584	0.5625	0.004921	0.1804
9.7 ……	0.002816	0.1456	0.5967	0.3839	0.003359	0.1545	0.4731	0.5626	0.005846	0.1856	0.002816	0.1456	0.5967	0.3839	0.003542	0.1597	0.4579	0.5617	0.006905	0.2018
9.8 ……	0.003941	0.1628	0.5961	0.383	0.004704	0.1727	0.4726	0.5616	0.008194	0.2076	0.003941	0.1628	0.5961	0.383	0.004959	0.1786	0.4574	0.5607	0.009673	0.2256
9.9 ……	0.005504	0.1819	0.5954	0.382	0.006573	0.1929	0.4719	0.5604	0.01146	0.232	0.005504	0.1819	0.5954	0.382	0.00693	0.1995	0.4567	0.5596	0.01352	0.252
10 ……	0.00767	0.203	0.5946	0.3807	0.009165	0.2154	0.4711	0.5591	0.016	0.2589	0.00767	0.203	0.5946	0.3807	0.009662	0.2227	0.456	0.5582	0.01887	0.2812
10.1 …..	0.01066	0.2263	0.5936	0.3792	0.01275	0.2401	0.4702	0.5575	0.02228	0.2887	0.01066	0.2263	0.5936	0.3792	0.01344	0.2484	0.455	0.5567	0.02625	0.3135
10.2 …..	0.01477	0.252	0.5924	0.3774	0.01767	0.2674	0.469	0.5557	0.03093	0.3215	0.01477	0.252	0.5924	0.3774	0.01863	0.2766	0.454	0.5548	0.03639	0.3489
10.3 …..	0.02039	0.2802	0.591	0.3754	0.02442	0.2974	0.4678	0.5536	0.04278	0.3575	0.02039	0.2802	0.591	0.3754	0.02574	0.3076	0.4527	0.5528	0.05027	0.3878
10.4 …..	0.02805	0.311	0.5894	0.3732	0.03362	0.3303	0.4663	0.5513	0.05893	0.3968	0.02805	0.311	0.5894	0.3732	0.03544	0.3416	0.4513	0.5504	0.06915	0.4301
10.5 …..	0.03842	0.3447	0.5876	0.3706	0.0461	0.3661	0.4647	0.5487	0.08081	0.4395	0.03842	0.3447	0.5876	0.3706	0.04859	0.3786	0.4497	0.5479	0.09465	0.476
10.6 …..	0.05239	0.3814	0.5856	0.3679	0.06292	0.405	0.4628	0.5459	0.1102	0.4858	0.05239	0.3814	0.5856	0.3679	0.06631	0.4189	0.448	0.5451	0.1289	0.5257
10.7 …..	0.07111	0.4211	0.5833	0.3649	0.08548	0.4472	0.4608	0.5429	0.1496	0.5356	0.07111	0.4211	0.5833	0.3649	0.09006	0.4624	0.446	0.5422	0.1744	0.5789
10.8 …..	0.09605	0.464	0.5809	0.3617	0.1155	0.4927	0.4587	0.5398	0.2017	0.5888	0.09605	0.464	0.5809	0.3617	0.1217	0.5094	0.4439	0.5392	0.2345	0.6358
10.9 …..	0.1291	0.5101	0.5782	0.3584	0.1553	0.5416	0.4564	0.5366	0.2702	0.6456	0.1291	0.5101	0.5782	0.3584	0.1636	0.5599	0.4417	0.5361	0.3113	0.6946
11 ……	0.1725	0.5595	0.5753	0.355	0.2077	0.5939	0.454	0.5334	0.3596	0.7056	0.1725	0.5595	0.5753	0.355	0.2187	0.6139	0.4394	0.533	0.408	0.7548
11.1 …..	0.2294	0.6123	0.5723	0.3515	0.2762	0.6495	0.4515	0.5302	0.4744	0.7684	0.2294	0.6123	0.5723	0.3515	0.2903	0.6709	0.4371	0.5302	0.5315	0.8177
11.2 …..	0.3033	0.6684	0.5692	0.348	0.3652	0.7085	0.4489	0.5271	0.6178	0.8323	0.3033	0.6684	0.5692	0.348	0.3833	0.7313	0.4347	0.5275	0.6905	0.884
11.3 …..	0.399	0.7278	0.566	0.3445	0.48	0.7708	0.4463	0.5241	0.8018	0.8996	0.399	0.7278	0.566	0.3445	0.5024	0.7945	0.4323	0.5255	0.8932	0.9536
11.4 …..	0.5219	0.7906	0.5627	0.3412	0.6266	0.8358	0.4437	0.5216	1.036	0.9699	0.5219	0.7906	0.5627	0.3412	0.6542	0.8604	0.43	0.5237	1.15	1.026
11.5 …..	0.679	0.8565	0.5594	0.3379	0.8118	0.9031	0.4412	0.5199	1.331	1.043	0.679	0.8565	0.5594	0.3379	0.8478	0.9294	0.4278	0.5219	1.472	1.101
11.6 …..	0.8779	0.9251	0.5561	0.3352	1.047	0.9733	0.4388	0.5181	1.702	1.119	0.8779	0.9251	0.5561	0.3352	1.093	1.001	0.4255	0.5201	1.874	1.178
11.7 …..	1.128	0.996	0.553	0.333	1.343	1.046	0.4365	0.5163	2.166	1.197	1.128	0.996	0.553	0.333	1.402	1.076	0.4233	0.5184	2.373	1.258
11.8 …..	1.443	1.07	0.55	0.3307	1.715	1.122	0.4341	0.5145	2.741	1.277	1.443	1.07	0.55	0.3307	1.789	1.154	0.4211	0.5167	2.99	1.34
11.9 …..	1.837	1.146	0.547	0.3284	2.179	1.2	0.4318	0.5127	3.453	1.36	1.837	1.146	0.547	0.3284	2.272	1.233	0.419	0.5152	3.75	1.423
12 ……	2.327	1.225	0.5441	0.3262	2.755	1.281	0.4295	0.511	4.303	1.442	2.327	1.225	0.5441	0.3262	2.871	1.316	0.4168	0.5137	4.68	1.509
12.1 …..	2.934	1.306	0.5412	0.324	3.468	1.364	0.4273	0.5094	5.306	1.522	2.934	1.306	0.5412	0.324	3.61	1.4	0.4147	0.5123	5.818	1.596
12.2 …..	3.682	1.39	0.5383	0.3219	4.344	1.448	0.425	0.5077	6.522	1.603	3.682	1.39	0.5383	0.3219	4.519	1.486	0.4126	0.5109	7.203	1.684
12.3 …..	4.6	1.475	0.5355	0.3197	5.403	1.533	0.4229	0.5068	7.986	1.685	4.6	1.475	0.5355	0.3197	5.63	1.574	0.4105	0.5095	8.886	1.775
12.4 …..	5.72	1.562	0.5327	0.3176	6.671	1.617	0.4208	0.5068	9.724	1.766	5.72	1.562	0.5327	0.3176	6.983	1.664	0.4085	0.5081	10.93	1.866
12.5 …..	7.071	1.649	0.53	0.3161	8.202	1.702	0.4189	0.5067	11.8	1.848	7.082	1.651	0.5299	0.3155	8.626	1.754	0.4064	0.5065	13.39	1.96
12.6 …..	8.686	1.736	0.5275	0.3152	10.04	1.787	0.417	0.5065	14.27	1.929	8.729	1.74	0.527	0.3133	10.61	1.847	0.4043	0.5049	16.37	2.054
12.7 …..	10.62	1.822	0.5251	0.3143	12.23	1.871	0.4152	0.5064	17.18	2.01	10.71	1.831	0.5242	0.311	13	1.94	0.4021	0.503	19.96	2.15
12.8 …..	12.93	1.908	0.5228	0.3134	14.83	1.955	0.4134	0.5063	20.6	2.09	13.09	1.923	0.5213	0.3086	15.86	2.034	0.3999	0.5009	24.29	2.248
12.9 …..	15.67	1.993	0.5206	0.3125	17.9	2.038	0.4116	0.5059	24.57	2.168	15.93	2.015	0.5183	0.3061	19.29	2.129	0.3976	0.4985	29.48	2.347
13 ……	18.9	2.078	0.5183	0.3116	21.53	2.12	0.4098	0.5054	29.15	2.244	19.3	2.108	0.5153	0.3033	23.36	2.224	0.3952	0.4958	35.73	2.448
13.1 …..	22.69	2.161	0.5161	0.3104	25.76	2.201	0.4079	0.5049	34.37	2.316	23.28	2.2	0.5121	0.3004	28.19	2.32	0.3927	0.4928	43.22	2.551
13.2 …..	27.12	2.242	0.5139	0.3092	30.67	2.279	0.406	0.5044	40.27	2.384	27.97	2.293	0.5089	0.2972	33.9	2.417	0.3901	0.4893	52.21	2.656
13.3 …..	32.27	2.322	0.5116	0.3078	36.33	2.354	0.404	0.5039	46.99	2.449	33.46	2.385	0.5054	0.2937	40.62	2.513	0.3873	0.4853	62.98	2.762
13.4 …..	38.2	2.399	0.5093	0.3066	42.8	2.426	0.402	0.5038	54.61	2.511	39.88	2.477	0.5018	0.29	48.52	2.61	0.3844	0.481	75.88	2.87
13.5 …..	45.05	2.472	0.5069	0.3056	50.18	2.494	0.4001	0.5042	63.25	2.569	47.37	2.569	0.4981	0.2862	57.81	2.708	0.3813	0.4765	91.32	2.981
13.6 …..	52.85	2.542	0.5046	0.3048	58.56	2.557	0.3982	0.5045	72.97	2.624	56.06	2.66	0.4942	0.2821	68.68	2.806	0.3782	0.4714	109.8	3.093
13.7 …..	61.72	2.608	0.5024	0.3044	68.09	2.618	0.3963	0.5049	83.87	2.675	66.14	2.752	0.4901	0.2779	81.38	2.905	0.375	0.466	131.9	3.208
13.8 …..	71.81	2.67	0.5002	0.3042	78.88	2.674	0.3945	0.5055	96.04	2.722	77.81	2.842	0.4859	0.2735	96.2	3.004	0.3716	0.4604	158.4	3.326
13.9 …..	83.26	2.728	0.4982	0.3041	91.07	2.727	0.3928	0.5062	109.6	2.765	91.29	2.933	0.4816	0.2689	113.5	3.104	0.3682	0.4544	190	3.446
14 ……	96.2	2.781	0.4962	0.3042	104.8	2.775	0.3911	0.507	124.6	2.804	106.8	3.024	0.4772	0.2642	133.6	3.204	0.3647	0.4481	227.8	3.568
14.1 …..	110.8	2.831	0.4944	0.3043	120.1	2.819	0.3895	0.5079	141.3	2.839	124.7	3.114	0.4727	0.2593	157	3.306	0.3612	0.4415	273	3.694
14.2 …..	127.2	2.876	0.4926	0.3045	137.3	2.859	0.388	0.509	159.6	2.87	145.2	3.205	0.468	0.2542	184.1	3.408	0.3575	0.4345	327.1	3.823
14.3 …..	145.5	2.917	0.491	0.3049	156.4	2.894	0.3865	0.5102	179.9	2.897	168.7	3.295	0.4633	0.2489	215.5	3.511	0.3538	0.4271	391.8	3.955
14.4 …..	166	2.954	0.4894	0.3054	177.5	2.925	0.3851	0.5115	202.3	2.92	195.5	3.386	0.4584	0.2435	251.8	3.615	0.3499	0.4195	469.1	4.091

[a] Mass in Earth mass ($M_{\oplus} = 5.9742 \times 10^{24}$ kg).

[b] Radius in Earth radius ($R_{\oplus} = 6.371 \times 10^{6}$ m).

[c] CRF stands for core radius fraction, the ratio of the radius of the core over the total radius of the planet, in the two-layer model.

[d] $p1/p0$ stands for core–mantle-boundary pressure fraction, the ratio of the pressure at the core–mantle boundary ($p1$) over the pressure at the center of the planet ($p0$), in the two-layer model.

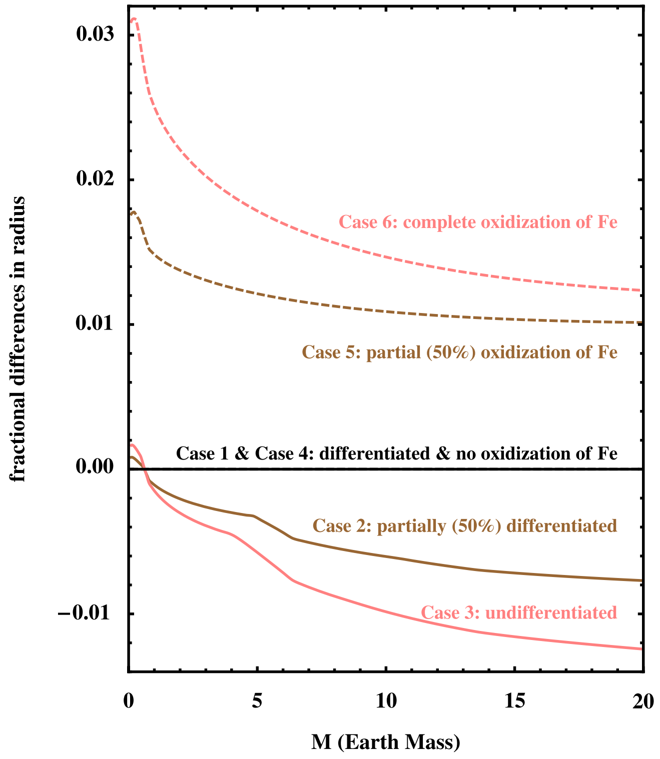

FIG. 4.—Fractional differences in radius resulting from Fe partitioning between mantle and core. Case 1 and Case 4 (complete differentiation and no oxidization of Fe, *black*); Case 2 (partial [50%] differentiation: 50% metallic Fe mixed with the mantle, *solid brown*); Case 3 (no differentiation: all metallic Fe mixed with the mantle, *pink*); Case 5 (partial [50%] oxidization of Fe, *dashed brown*); Case 6 (complete oxidization of Fe, *dashed pink*). See the online edition of the *PASP* for a color version of this figure.

scale. And the range between 10 and 100 $M_\oplus$ is equally divided into 10 sections in logarithmic scale.

2. *Radius*: For each mass M in Table 3 there are 12 radius values, 11 of which are equally spaced within the allowed range: $R_{\mathrm{Fe}}(M) + (R_{\mathrm{H_2O}}(M) - R_{\mathrm{Fe}}(M)) * i$, where $i = 0, 0.1, 0.2, \ldots, 0.9, 1.0$. The 12th radius value ($R_{\mathrm{MgSiO_3}}(M)$) is inserted into the list corresponding to the pure-$MgSiO_3$ planet radius (see Table 1) for mass M. Here $R_{\mathrm{Fe}}(M)$, $R_{\mathrm{MgSiO_3}}(M)$, and $R_{\mathrm{H_2O}}(M)$ are the radii for planets with mass M composed of pure-Fe, pure-$MgSiO_3$, and pure-H_2O correspondingly.

Overall, there are $41 * 12 = 492$ different mass–radius pairs in Table 3. For each (M, R), three cases: $p0_{\mathrm{min}}$, $p0_{\mathrm{mid}}$, and $p0_{\mathrm{max}}$ are listed.

3. Central pressure $p0$ (Pascal) in logarithmic base-10 scale.

4. $p1/p0$, the ratio of $p1$ (the first boundary pressure, i.e., the pressure at the Fe-$MgSiO_3$ boundary) over $p0$.

5. $p2/p1$, the ratio of $p2$ (the second boundary pressure, i.e., the pressure at the $MgSiO_3$-H_2O boundary) over $p1$.

6. Fe mass fraction (the ratio of the Fe-layer mass over the total mass of the planet).

7. $MgSiO_3$ mass fraction (the ratio of the $MgSiO_3$-layer mass over the total mass of the planet).

8. H_2O mass fraction (the ratio of the H_2O-layer mass of over the total mass of the planet).

The sixth, seventh and eighth columns always add up to one.

A dynamic and interactive tool to characterize and illustrate the interior structure of exoplanets built upon Table 3 and other models in this article is available online (see [1]).

TABLE 3

TABLE FOR TERNARY DIAGRAM

$M(M_\oplus)$	$R(R_\oplus)$	$\log_{10}(p0)$	$p1/p0$	$p2/p1$	Fe	$MgSiO_3$	H_2O
0.1	0.3888	10.9212	0	0	1	0	0
0.1	0.3888	10.9212	0	0	1	0	0
0.1	0.3888	10.9212	0	0	1	0	0
0.1	0.4226	10.9066	0.133	0	0.759	0.241	0
0.1	0.4226	10.9126	0.102	0.046	0.818	0.172	0.01
0.1	0.4226	10.9186	0.024	1	0.953	0	0.047
⋮	⋮	⋮	⋮	⋮	⋮	⋮	⋮
100	4.102	13.0979	1	1	0	0	1

NOTE.—Table is shown in its entirety in the electronic edition of the *PASP*. A portion is shown here regarding its form and content.

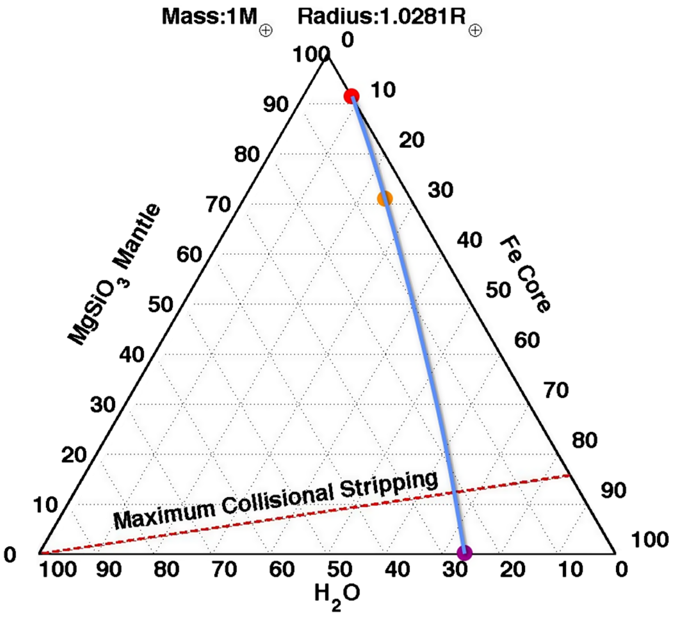

FIG. 5.—The *red*, *orange* and *purple points* correspond to $\log_{10}(p0\,(\mathrm{in}\,Pa)) = 11.4391$, 11.5863, and 11.7336. The mass fractions are (1) $\mathrm{FeMF} = 0.083$, $\mathrm{MgSiO_3MF} = 0.917$, $\mathrm{H_2OMF} = 0$ (*red*); (2) $\mathrm{FeMF} = 0.244$, $\mathrm{MgSiO_3MF} = 0.711$, $\mathrm{H_2OMF} = 0.046$ (*orange*); (3) $\mathrm{FeMF} = 0.728$, $\mathrm{MgSiO_3MF} = 0$, $\mathrm{H_2OMF} = 0.272$ (*purple*). MF here stands for mass fraction. The *blue curve* is the parabolic fit. The *red dashed curve* is the maximum collisional stripping curve by Marcus et al. (2010). See the online edition of the *PASP* for a color version of this figure.

4.5. Generate Curve Segment on Ternary Diagram Using Table 3

One utility of Table 3 is to generate the curve segment on the three-layer ternary diagram for a given mass–radius pair. As an example, for $M = 1\ M_\oplus$ and $R = 1.0281\ R_\oplus$, the table provides three $p0$s. For each $p0$, the mass fractions of Fe, $MgSiO_3$, and H_2O are given to determine a point on the ternary diagram. Then, a parabolic fit (see Fig. 5) through the three points is a good approximation to the actual curve segment. This parabola may intersect the maximum collisional stripping curve by Marcus et al. (2010), indicating that the portion of parabola beneath the intersection point may be ruled out by planet formation theory.

5. CONCLUSION

The two-layer and three-layer models for solid exoplanets composed of Fe, $MgSiO_3$, and H_2O are the focus of this article. The mass–radius contours (Fig. 2) are provided for the two-layer model, useful for readers to quickly calculate the interior structure of a solid exoplanet. The two-parameter contour mesh may also help one build physical insights into the solid exoplanet interior structure.

The complete three-layer mass–fraction ternary diagram is tabulated (Table 3), useful for readers to interpolate and calculate all solutions as the mass fractions of the three layers for a given mass–radius input. The details of the EOS of Fe, $MgSiO_3$, and H_2O and how they are calculated and used in this article are discussed in § 3 and shown in Figure 1.

A dynamic and interactive tool to characterize and illustrate the interior structure of exoplanets built upon Table 3 and other models in this article is available online (see [1]).

The effect of Fe partitioning between mantle and core on mass–radius relation is explored in § 4.3, and the result is shown in Figure 4 and Table 2.

With the ongoing *Kepler* Mission and many other exoplanet searching projects, we hope this article could provide a handy tool for observers to fast characterize the interior structure of exoplanets already discovered or to be discovered, and further our understanding of those worlds beyond our own.

We acknowledge partial support for this work by NASA cooperative agreement NNX09AJ50A (*Kepler* Mission science team).

We would like to thank Michail Petaev and Stein Jacobsen for their valuable comments and suggestions. This research is supported by the National Nuclear Security Administration under the High Energy Density Laboratory Plasmas through DOE grant # DE-FG52-09NA29549 to S. B. Jacobsen (PI) with Harvard University. This research is the authors' views and not those of the DOE.

Li Zeng would like to thank Professor Pingyuan Li, Li Zeng's grandfather, in the Department of Mathematics at Chongqing University, for giving Li Zeng important spiritual support and guidance on research. The guidance includes research strategy and approach, methods of solving differential equations and other numeric methods, etc.

Li Zeng would also like to give special thanks to Master Anlin Wang. Master Wang is a Traditional Chinese Kung Fu Master and World Champion. He is also a practitioner and realizer of Traditional Chinese Philosophy of Tao Te Ching, which is the ancient oriental wisdom to study the relation between the universe, nature and humanity. Valuable inspirations were obtained through discussion of Tao Te Ching with Master Wang as well as Qigong cultivation with him.

REFERENCES

Anderson, O. L., Dubrovinsky, L., Saxena, S. K., & LeBihan, T. 2001, Geophys. Res. Lett., 28, 399
Asplund, M., Grevesse, N., Sauval, A. J., & Scott, P. 2009, ARA&A, 47, 481
Batalha, N. M., Borucki, W. J., BrysonS. T.et al. 2011, ApJ, 729, 27
Bina, C. 2003, in Treatise on Geochemistry, ed. H. D. Holland, & K. K. Turekian (Oxford: Pergamon), 39
Birch, F. 1947, Phys. Rev., 71, 809
Borucki, W. J., Koch, D. G., Batalha, N., et al. 2012, ApJ, 745, 120
Caracas, R., & Cohen, R. E. 2008, Phys. Earth Planet. Inter., 168, 147
Carter, J. A., Agol, E., ChaplinW. J., et al. 2012, Science, 337, 556
Chaplin, M. 2012, Water Phase Diagram, http://www.lsbu.ac.uk/water/phase.html#bb
Charbonneau, D., Berta, Z. K., Irwin, J., et al. 2009, Nature, 462, 891
Choukroun, M., & Grasset, O. 2007, J. Chem. Phys., 127, 124506
Cochran, W. D., Fabrycky, D. C., Torres, G., et al. 2011, ApJS, 197, 7
Daucik, K., & Dooley, R. B. 2011, Revised Release on the Pressure along the Melting and Sublimation Curves of Ordinary Water Substance (The International Association for the Properties of Water and Steam)
Dunaeva, A. N., Antsyshkin, D. V., & Kuskov, O. L. 2010, Sol. Syst. Res., 44, 202
Eliezer, S., Ghatak, A., & Hora, H. 2002, Fundamentals of Equations of State (London: World Scientific)
Fei, Y., Zhang, L., Corgne, A., et al. 2007, Geophys. Res. Lett., 34, L17307
Fortney, J., Marley, M., & Barnes, J. 2007, ApJ, 659, 1661
Frank, M. R., Fei, Y., & Hu, J. 2004, Geochim. Cosmochim. Acta, 68, 2781 (FFH2004)
French, M., Mattsson, T. R., Nettelmann, N., & Redmer, R. 2009, Phys. Rev. B, 79, 054107 (FMNR2009)
Fressin, F., Torres, G., Rowe, J. F., et al. 2012, Nature, 482, 195
Gautier, T. N., III, Charbonneau, D., et al. 2012, ApJ, 749, 15
Goncharov, A. F., Goldman, N., Fried, L. E., et al. 2005, Phys. Rev. Lett., 94, 125508
Grasset, O., Schneider, J., & Sotin, C. 2009, ApJ, 693, 722
Hatzes, A. P., Fridlund, M., Nachmani, G., et al. 2011, ApJ, 743, 75
Hirose, K. 2010, Sci. Am., 302, 76
Hirsch, K., & Holzapfel, W. 1984, Phys. Lett. A, 101, 142
Howell, S. B., Rowe, J. F., Bryson, S. T., et al. 2012, ApJ, 746, 123

Karki, B. B., Wentzcovitch, R. M., de Gironcoli, S., & Baroni, S. 2000, Phys. Rev. B, 62, 14750

Kresse, G., & Furthmüller, J. 1996, Phys. Rev. B, 54, 11169

Kresse, G., & Hafner, J. 1993, Phys. Rev. B, 47, 558

———. 1994, J. Phys. Condensed Matter, 6, 8245

Leger, A., Rouan, D., Schneider, J., et al. 2009, A&A, 506, 287

Lissauer, J. J., Fabrycky, D. C., Ford, E. B., et al. 2011, Nature, 470, 53

Macfarlane, J. J. 1984, ApJ, 280, 339

Marcus, R., Sasselov, D., Hernquist, L., & Stewart, S. 2010, ApJ, 712, L73

Murakami, M., Hirose, K., Kawamura, K., Sata, N., & Ohishi, Y. 2004, Science, 304, 855

Oganov, A. R., & Ono, S. 2004, Nature, 430, 445

Poirier, J.-P. 2000, Introduction to the Physics of the Earth's Interior (Cambridge, UK: Cambridge University Press)

Queloz, D., Bouchy, F., Moutou, C., Hatzes, A., & Hébrard, G. 2009, A&A, 506, 303

Robinson, G. W., Zhu, S. B., Singh, S., & Evans, M. W. 1996, Water in Biology, Chemistry and Physics: Experimental Overviews and Computational Methodologies (Singapore: World Scientific)

Salpeter, E. E., & Zapolsky, H. S. 1967, Phys. Rev., 158, 876

Seager, S., Kuchner, M., Hier-Majumder, C. A., & Militzer, B. 2007, ApJ, 669, 1279 (SKHMM2007)

Sotin, C., Grasset, O., & Mocquet, A. 2007, Icarus, 191, 337

Sotin, C., Jackson, J. M., & Seager, S. 2010, Exoplanets (Tuscon: The University of Arizona Press), 375–395

Spera, F. J., Yuen, D. A., & Giles, G. 2006, Phys. Earth Planet. Inter., 159, 234

Stixrude, L., & Lithgow-Bertelloni, C. 2011, Geophys. J. Int., 184, 1180

Swift, D. C., Eggert, J. H., Hicks, D. G., et al. 2012, ApJ, 744, 59

Umemoto, K., & Wentzcovitch, R. M. 2011, Earth Planet. Sci. Lett., 311, 225

Valencia, D., Ikoma, M., Guillot, T., & Nettelmann, N. 2010, A&A, 516A20

Valencia, D., O'Connell, R. J., & Sasselov, D. 2006, Icarus, 181, 545

Valencia, D., Sasselov, D. D., & O'Connell, R. J. 2007a, ApJ, 665, 1413

———. 2007b, ApJ, 656, 545

Vinet, P., Ferrante, J., Rose, J. H., & Smith, J. R. 1987, J. Geophys. Res., 92, 9319

Vinet, P., Rose, J. H., Ferrante, J., & Smith, J. R. 1989, J. Phys. Condensed Matter, 1, 1941

Wagner, F. W., Sohl, F., Hussmann, H., Grott, M., & Rauer, H. 2011, Icarus, 214, 366

Winn, J. N., Matthews, J. M., Dawson, R. I., Fabrycky, D., & Holman, M. J. 2011, ApJL, 737, L18

Wu, S., Umemoto, K., Ji, M., et al. 2011, Phys. Rev. B, 83, 184102

Yu, G., & Jacobsen, S. B. 2011, PNAS, 108, 17604

Zeng, L., & Seager, S. 2008, PASP, 120, 983